Heliyon 10 (2024) e38027

Contents lists available at ScienceDirect

Heliyon

journal homepage: www.cell.com/heliyon

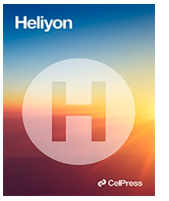

Research article

An improved semi-supervised segmentation of the retinal vasculature using curvelet-based contrast adjustment and generalized linear model

Feudjio Ghislain [a,b,*], Saha Tchinda Beaudelaire [b], Tchiotsop Daniel [b]

[a] *Research Unit of Condensed Matter, Electronics and Signal Processing (UR-MACETS). Department of Physics, Faculty of Sciences, University of Dschang, P.O. Box 67, Dschang, Cameroon*

[b] *Research Unit of Automation and Applied Computer (UR-AIA), Electrical Engineering Department of IUT-FV, University of Dschang, P.O. Box: 134, Bandjoun, Cameroon*

ARTICLE INFO

Keywords:
Retinal blood vessel
Curvelet transform
Gabor filters
Image segmentation
Generalized linear model

ABSTRACT

Diagnosis of most ophthalmic conditions, such as diabetic retinopathy, generally relies on an effective analysis of retinal blood vessels. Techniques that depend solely on the visual observation of clinicians can be tedious and prone to numerous errors. In this article, we propose a semi-supervised automated approach for segmenting blood vessels in retinal color images. Our method effectively combines some classical filters with a Generalized Linear Model (GLM). We first apply the Curvelet Transform along with the Contrast-Limited Histogram Adaptive Equalization (CLAHE) technique to significantly enhance the contrast of vessels in the retinal image during the preprocessing phase. We then use Gabor transform to extract features from the enhanced image. For retinal vasculature identification, we use a GLM learning model with a simple link identity function. Binarization is then performed using an automatic optimal threshold based on the maximum Youden index. A morphological cleaning operation is applied to remove isolated or unwanted segments from the final segmented image. The proposed model is evaluated using statistical parameters on images from three publicly available databases. We achieve average accuracies of 0.9593, 0.9553 and 0.9643, with Receiver Operating Characteristic (ROC) analysis yielding Area Under Curve (AUC) values of 0.9722, 0.9682 and 0.9767 for the CHASE_DB1, STARE and DRIVE databases, respectively. Compared to some of the best results from similar approaches published recently, our results exceed their performance on several datasets.

1. Introduction

Changes in the retinal vasculature, such as microaneurysms, hemorrhages, and increased levels of vascular tortuosity, are often indicators of conditions like diabetic retinopathy, stroke and other vascular disorders [1–5]. Manual analysis of retinal images for the diagnostic of these diseases is both tedious and requires extensive expertise. Therefore, the automatic image analysis is essential for decision-making [6–13]. Typically, the implementation of an automatic image analysis system involves several phases, including denoising, edge detection or segmentation [14–19]. The effectiveness of these systems in preventing, diagnosing, or treating the

* Corresponding author.
E-mail address: feudjioghislain@gmail.com (F. Ghislain).

https://doi.org/10.1016/j.heliyon.2024.e38027
Received 17 February 2024; Received in revised form 12 August 2024; Accepted 16 September 2024
Available online 17 September 2024

associated pathologies depends heavily on the accuracy of the segmentation processes. Consequently, the development of algorithms that improve the accuracy of retinal vessels detection remains a significant research challenge.

Many revolutionary segmentation techniques have been proposed to date, generally categorized into supervised or unsupervised approaches [20–33]. Supervised approaches typically rely on automated learning concepts, including Machine Learning (ML) or Deep Learning (DL). These methods use artificial neural networks to create classifiers that distinguish between pixels characteristic of vessels and non-vessels in retinal images. Classifiers are trained using a set of features extracted from images previously labeled by experts as either belonging to the vascular system or not. The vessel identification process relies on algorithms trained with these labeled images to accurately detect and segment the retinal vasculature. Supervised techniques generally offer high precision but can be challenging to implement due to their need for extensive training databases with a large number of images. Additionally, they require managing of multiple features and classifiers which imposes a significant computational load.

In contrast, unsupervised methods use models that incorporate multi-scale or morphological analyzes and adaptive filters to extract the vascular network from retinal images [6–12]. Each image is segmented independently, typically following several preprocessing steps and subsequent post-processing. While these methods are easier to implement and more effective at extracting thicker vessels with better precision, they usually have lower performance for segmenting thinner vessels compared to supervised techniques. Comparative data on the advantages and disadvantages of both categories of techniques can be found in Refs. [9,32].

Despite recent advances in segmentation approaches, their implementation remains challenging due to several factors. The quality of the results can be affected by issues such as noise during acquisition, compression errors, low contrast, non-uniform illumination, and variations in vessel width, which can lead to discontinuities and undesirable pixels [10–12,14]. Moreover, the uniqueness of the retinal morphology in each individual, whether healthy or diseased, along with unpredictable changes or lesions caused by various pathologies, affect the segmentation performance of even supervised methods. Implementing a training set that encompasses all necessary data to account for these diverse conditions is challenging, which limits the capacity of classifiers and, consequently, the overall performance of the proposed systems [15–33]. The main challenge is to develop a segmentation approach that is both easy to implement and capable of ensuring high accuracy in detecting retinal blood vessels, regardless of image quality or variability in observable changes.

In this work, we propose a new hybrid model for automated and accurate segmentation of retinal vascular structures. This model leverages the strengths of both supervised and unsupervised approaches. The approach focuses on enhancing the pre-processing and post-processing phases using traditional unsupervised techniques to effectively remove unconnected or unwanted components from the detected vascular system. Between these phases, the accuracy of thin vessel segmentation is improved by incorporating a supervised intermediate step, which uses only a portion of the image features for training [34–37].

Initially, we exploit the advantages of the Fast Discrete Curvelet Transform (FDCT) to enhance preprocessing quality, combining it with the Contrast-Limited Adaptive Histogram Equalization (CLAHE) technique. The digital implementation of FDCT addresses the limitations of other multiresolution techniques by effectively highlighting object contours in images with strong anisotropy [14–19]. This approach improves image quality while preserving its complex structures [38–41]. The integration of FDCT with the widely used CLAHE technique has optimized preprocessing performance, demonstrating a significant impact on enhancing the accuracy of the final segmentation [42,43].

The main features of each enhanced image are further extracted using Gabor wavelet transforms and then used as inputs to a Generalized Linear Model (GLM) with a simple identity link function and a regular distribution of the output response. Only half of the extracted features are utilized for training the model, while the remaining features are reserved for testing. Binarization is performed using an automatic optimal threshold determined by maximizing the Youden index. Finally, a morphological cleaning operation is applied to remove unconnected or unwanted pixels from the segmented image. We evaluated the model's performance by computing several statistical and graphical measurement parameters using images from the CHASE_DB1, DRIVE and STARE databases. The accuracy (Acc), specificity (Sp), sensitivity (Se), and Area Under the Receiver Operating Characteristic Curve (AUC) were compared to the results from several recently published similar works to demonstrate the robustness and reliability of our algorithm.

In the following section, we review recent previous studies on retinal blood vessels segmentation. Section 3 presents materials and details of the methodology used in this article. Section 4 discusses the experimental results obtained with our model and compares them to recent methods. Finally, we conclude this work in section 5.

2. Previous works

Retinal images are often affected by various types of noise, such as Poisson noise or Gaussian noise, which arise from sensor imperfections or digitization defects. To improve the quality of these images, it is crucial to apply preprocessing techniques such as illumination uniformization and artifact correction. Common methods include mean, median, and Gaussian filters, as well as contrast enhancement techniques like histogram equalization [10]. Several studies have clearly demonstrated the impact of appropriate preprocessing on the final accuracy of retinal blood vessel segmentation [12,16]. Some preprocessing techniques often involve contrast enhancement through various transforms in the spatial, frequency, or temporal domains. One notable enhancement method is contrast adjustment using wavelets, which leverages time-frequency multiresolution analysis [14–18]. Asem et al. [14] utilized these multiresolution techniques to denoise images. Compared to spatial improvement methods, Zhen et al. [15], Bankhead et al. [17], and Zhang et al. [18] have shown that wavelet transforms can significantly enhance edge highlighting and overall image quality.

However, these transforms have faced difficulties in describing objects with significant anisotropy. The Curvelet Transform was designed to better overcome the limitations of the separable wavelet transform in representing curves and edges. It has achieved significant success in various image processing tasks, such as improving image quality. The Curvelet transform is localized in the

directional, frequency, and spatial domains, and it exhibits high directional or anisotropic sensitivity [19]. One of its variants, known as the Fast Discrete Curvelet Transform (FDCT), is characterized by its ability to efficiently represent object boundaries, lines, curves, and edges in many directions. This variant was employed by Rahulkar et al. [39] for image feature extraction, and by Altan et al. [41] as a crucial method for image contrast enhancement in conjunction with other models. With the aim of further improving segmentation accuracy, several authors, including Soares et al. [28], Aslan et al. [29], and Fang et al. [32], have successfully utilized image transformation techniques involving filters or Gabor wavelets. Note that Gabor filters can be defined as the product of a sinusoidal or harmonic function and a Gaussian function. Considered as edge, line, or shape detectors, the main characteristic of these filters is their ability to adapt to different frequencies and orientations [44,45].

Overall, the segmentation techniques for the vascular system are summarized into two broad categories: supervised and unsupervised techniques [16–33,46–70]. Unsupervised approaches do not require prior training data. They rely on the application of various morphological functions to analyze and segment retinal images. Tavakoli et al. [3] presented an unsupervised automated approach for extracting the retinal vasculature, utilizing morphological operators during the preprocessing phase to enhance the structural network of blood vessels. The main processing phase involves applying the Radon transform to overlapping windows. Finally, they refined and reconstructed the vessels to achieve the final binarization. Dash and Bhoi [8] implemented a recursive approach to ophthalmoscopic image segmentation by applying a vessel enhancement technique with CLAHE, preceded by gamma correction. They then used an iterative adaptive thresholding method to extract blood vessels. The final segmented images, with appreciable average precision, were obtained using a morphological cleaning operation.

Ravichandran et al. [10] presented a fully automatic approach for blood vessel extraction using enhancement and thresholding techniques. The input image is improved through histogram matching and CLAHE methods. They employed Wiener filtering to remove background noise. To finally extract the retinal vasculature from Gabor filter responses of the CLAHE-enhanced image, a thresholding approach based on local entropy was applied. Saleh et al. [12] focused on major preprocessing algorithms, such as contrast enhancement and thresholding, to develop an automatic process for segmenting retinal vessels. Mean-C thresholding was used by Dash et al. [16] to segment the retinal vascular network, after enhancing the performance of the Curvelet Transform, by combining it with a Jerman filter. Dash et al. [33] combined a homomorphic filter with the CLAHE technique to extract the retinal vascular network while maintaining a low computational load.

Geethalakshmi et al. [35] explored another unsupervised technique for segmenting retinal vessels. This technique is based on CLAHE combined with median filtering methods to enhance the vascular network. The main segmentation phase was achieved using maximum principal curvature and various morphological functions. Jadoon et al. [49] and Nayab et al. [59] proposed unsupervised vessel segmentation approaches that also start with CLAHE-based contrast enhancement. Jadoon et al. [49] applied then the Top-Hat morphological operation for denoising, followed by High Boost and Frangi filters, and ISODATA thresholding to obtain the final binary image. Meanwhile, Nayab et al. [59] employed Gabor wavelets combined with an appropriate filter, followed by a human visual system (HVS) approach to achieve their results.

Among the supervised methods, Zhang et al. [18] proposed a retinal vessel binarization model that utilizes filtering techniques and wavelet transform. Specialized transformations are employed to optimize feature extraction with maximum orientation responses at various scales for vessels of different calibers. Finally, the vessels are segmented using a Random Forest classifier. Soares et al. [28] proposed characteristic vectors formed from pixel intensities, with scaled responses from the bidimensional Gabor wavelet applied to each set of pixels. They used a Bayesian Classifier with Gaussian Mixtures to classify the characteristic vector responses into vessel and non-vessel pixels.

Aslan et al. [29] obtained retinal vessels from original retinal images, using key features as input for an Extreme Learning Machine (ELM). During the feature extraction phase, they employed adaptive thresholding, Gabor, and Top-Hat transforms to enhance the vascular network. Boudegga et al. [30] proposed a U-shaped deep learning architecture based on simple convolutional blocks with the goal of maintaining high segmentation performance while minimizing computational load, after performing several preprocessing steps. Extensive reviews of supervised retinal image segmentation techniques using neural networks or their variants are provided in Refs. [20,22,25,46].

Supervised approaches, especially those based on deep learning, generally achieve superior segmentation accuracy compared to unsupervised methods. However, they are not always straightforward to implement due to the need for a large training dataset and significant processing load. To leverage the strengths of both approaches, several authors have combined them for an efficient dual-segmentation process [9,32]. Hashemzadeh et al. [9] implemented a range of relevant image features and a combination of training models for their hybrid segmentation approach. In the unsupervised phase, clear and thick blood vessels were initially identified, followed by a second supervised phase to detect thin vessels. The main features used for segmentation included the Top Hat transform, Shade Correction, Bit Plane Slicing, and Fuzzy C-Means clustering, among others. To obtain the final result, they performed a post-processing step that involved reducing the radius of the field of view (FOV) mask by a few pixels. In their proposed hybrid model, Fang et al. [32] first applied a supervised step based on a Generalized Linear Model (GLM) integrating the Gabor wavelet transform. The subsequent unsupervised step involved controlling lighting variations and adjusting detail magnification using the CLAHE technique.

As mentioned above, the major issues with several proposed methods are the complexity of implementation and the need to enhance the overall segmentation performance of the algorithm. Considering the advantages and limitations of supervised and/or unsupervised techniques, it is prudent to develop a hybrid model that leverages the strengths of both approaches while mitigating their drawbacks. This involves combining reliable segmentation with ease of system adaptation by further developing features that have demonstrated simplicity in implementation.

3. Materials and methods

Fig. 1 presents a synoptic of the proposed model. The overall process is divided into several stages: pre-processing, retinal blood vessels extraction, post-processing, and performance evaluation. Experiments with the developed algorithms were conducted using the MATLAB 2017b environment on a CPU Core i5 2.67 GHz processor with 8 GB of RAM.

3.1. Databases

The retina images used to validate the proposed algorithm were sourced from the publicly available CHASE_DB1, STARE and DRIVE databases.

The CHASE_DB1 dataset consists of 28 color images of the retina background, divided into two subsets of 14 images each. For each image in the database, two manual segmentation results were obtained from two independent experts. In this study, we used one of the subsets along with the segmentation results corresponding to the manual segmentation performed by the first expert for performance evaluation [3,8]. The DRIVE database contains 40 color photographs of retinal images: 33 from healthy retinas and 7 from abnormal retinas. The set of 40 photographs was divided into training and testing sets, each containing 20 images. These images are characterized by low uniform illumination of the background, less contrasting vessels, and a relatively large arteriole exhibiting a bright band widening towards the center. For each image in these datasets, two manual extraction results provided by different observers are available. The manual segmentation results from the first expert will be used as ground truth in this paper. The STARE database includes 20 color retinal photographs, half of which are normal and the other half abnormal [24–33]. This database also contains manual segmentation results for each image provided by an observer, which will be utilized as ground truth in this article.

3.2. Pre-processing

At the beginning of this stage, the color retinal image is split into red, green, and blue channels. Only the green channel is further used due to its superior contrast. Compared to the blue and red channels, the green channel of the color image provides better visualization and reveals the most distinct physiological structures, including blood vessels. The blue channel tends to exhibit more pronounced noise, while the red channel often fails to produce a clear image due to low saturation and contrast [34–36]. Because the green channel offers better contrast and produces images with higher intensity.

3.2.1. Fast discrete curvelet transform

The two-dimensional (2D) wavelet transform, commonly used in signal and image processing, has been extended by the curvelet

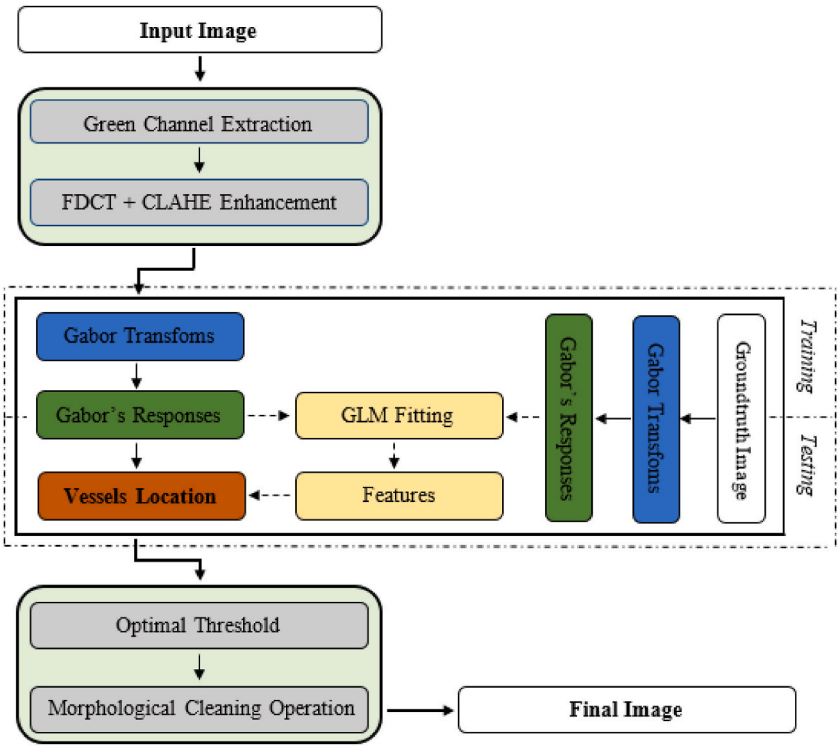

Fig. 1. Synoptic of the proposed model.

transform, which decomposes signals using a linear and weighted combination of basis functions called curvelets. The core idea is to partition an image into a fixed number of sub-bands, dividing the object into various scales and allowing each curvature to be represented by a relatively small number of coefficients [19]. The Fast Discrete Curvelet Transform (FDCT), also known as the second generation of the curvelet transform, is a refined variant of the original transform proposed by Candès et al. [40]. FDCT is based on a multi-scale and multi-dimensional image decomposition technique and is preferred for its simplicity or low redundancy [26]. There are two main digital implementation models for this curvelet: FDCT via the Unequally Spaced Fast Fourier Transform (FDCT-USFFT) and FDCT via Wrapping (FDCT-Wrap). In this paper, FDCT via Wrapping will be implemented as it proves to be efficient and faster than FDCT-USFFT [19,26,38–41].

The multi-scale decomposition of the original image is represented by the Fourier plane being divided into concentric circles in the wrapping method. Within each of these concentric circles, there are several angular divisions. These combinations of scale and angular divisions are referred to as parabolic wedges. This implementation relies on various Fourier sampling operations. When the system input is a 2D image represented as a Cartesian matrix $f[t_1, t_2]$ of MxN dimensions with $0 \le t_1 < M, 0 \le t_2 < N$, the coefficients of discrete curvelets $\boldsymbol{C^D(j,l,k)}$ corresponding to each corner are given by the following equation [38–41]:

$$\boldsymbol{C^D(j,l,k)} = \sum_{\boldsymbol{0 \le m,n < N}} \boldsymbol{f}[t_1, t_2]\overline{\boldsymbol{\varphi^D_{j,l,k}}[t_1, t_2]}. \tag{1}$$

where $\varphi^D_{j,l,k}$ is the digital waveform of the discrete curvelets; (j, l, k) designate scale, angle and orientation, respectively. These curvelet coefficients C are generated by two coordinate systems: one Polar and the other Cartesian. According to the polar coordinate system, we consider radial and an angular windows respectively W(r) and V(t), using for the first, positive real values with r ∈ [1/2; 2], and for the second, real values with t ∈ [-1; 1]. Equations (2) and (3) present the admissibility conditions of these window functions [40]:

$$\sum_{j=-\infty}^{+\infty} W^2\left(2^j r\right) = 1, r \in \left[\frac{3}{4}; \frac{3}{2}\right]. \tag{2}$$

$$\sum_{l=-\infty}^{+\infty} V^2(t-l) = 1, t \in \left[-\frac{1}{2}; \frac{1}{2}\right]. \tag{3}$$

In the Cartesian coordinate system, the frequencies isolated by the windows $\widetilde{\boldsymbol{U}}_{\boldsymbol{j,l}}$ around the different corners (ω_1, ω_2) are given by the following parameters [39,40]:

$$\widetilde{U}_{j,l} = W_j(\omega)V_j(\omega), \tag{4}$$

with

$$\begin{cases} W_j(\omega) = \sqrt{\varphi^2_{j+1}(\omega) - \varphi^2_j(\omega)}, j \ge 0 \\ V_j(\omega) = V\left(2^{j/2}\omega_1/\omega_2\right) \end{cases}.$$

The φ function is defined as coming from the 1D low-pass window:

$$\varphi_j(\omega_1, \omega_2) = \varnothing\left(2^{-j}\omega_1\right)\varnothing\left(2^{-j}\omega_2\right), 0 \le \varnothing \le 1.$$

Alternatively, instead of a slanted grid, one can assume an uniform rectangular lattice and determine the "Cartesian" curvelets rigorously in the same way as before as illustrated by the following equation [41]:

$$c(j,l,k) = \int \widetilde{f}(\omega)\widetilde{u}_j\left(S^{-1}_{\theta l}\omega\right)e^{\langle b,\omega\rangle}d\omega. \tag{5}$$

Note that the position b takes the digital values $\left(k_1.2^{-j}, k_1.2^{-j/2}\right)$ with $\theta\epsilon(-\pi/4, \pi/4)$. Considering $f[t_1, t_2]$ as an input Cartesian array and $\widetilde{f}[n_1, n_2]$ as a 2D discrete Fourier transform, FDCT-Wrap technique algorithm used for this study is developed as follows:

i. Obtain Fourier samples $\widetilde{f}[n_1, n_2]$ by applying the 2D fast Fourier transform (FFT) for input Cartesian array $f[t_1, t_2]$;
ii. Compute the product $\widetilde{U}_{j,l}[n_1, n_2]$*$\widetilde{f}[n_1, n_2]$ for each angle j and scale l, where $\widetilde{U}$ is a discrete cartesian windows;
iii. Obtain $\widetilde{f}_{j,l}[n_1, n_2] = W(\widetilde{U}_{j,l}\widetilde{f})(n_1, n_2)$ by wrapping the previous product around origin;
iv. Collect the discrete curvelet coefficients $C^D(j,l,k)$ by applying 2D inverse FFT to each obtained $\widetilde{f}_{j,l}$.

3.2.2. Image enhancement by CLAHE

The image histogram is a graphical representation of the intensity levels of the various data points in an image. This allows for modification to improve image quality. One of the most common techniques for this purpose is histogram equalization, valued for its simplicity of implementation [10]. In this stage, we implement a contrast enhancement method based on CLAHE (Contrast Limited Adaptive Histogram Equalization). This method is used to further enhance the contrast of the previous image. Since blood vessels are

key features in retinal images, the CLAHE method enables clearer visualization of these vessels compared to other methods. This enhancement process ensures an even distribution of intensity levels and adjusts the original image's contrast. The principle of CLAHE is based on a distribution function that enhances overall contrast in images where gray levels are overly concentrated in a specific range. It helps to minimize the enhancement of artifacts and noise that may result from the initial image acquisition [8,10,12,16,32,42].

3.3. Segmentation

3.3.1. Gabor wavelet transfom

In this study, blood vessel features are extracted from the previously enhanced retinal images using the Gabor wavelet transform. It is important to note that the Gabor wavelet transform is commonly used in the literature to identify multi-scale and multi-directional contours in images. This transform can be adjusted across specific frequencies, scales, and directions, making it effective as a background noise suppressor and low-level feature extractor. The filter was originally introduced by Dennis Gabor, and its impulse response is determined by the product of a complex sinusoid and a Gaussian kernel as follows [28,29,32,44,45,47,64,70]:

$$g_{\lambda,\theta,\varphi,\sigma,\gamma}(x,y) = exp\left\{ -0.5\left(\frac{x'^2+\gamma^2y'^2}{2\sigma^2}\right)\right\} exp\left\{i\left(2\pi\frac{x'}{\lambda}+\varphi\right)\right\}. \tag{6}$$

Real g^R and imaginary g^I components of this filter are defined as [32]:

$$g^R_{\lambda,\theta,\varphi,\sigma,\gamma}(x,y) = exp\left(-\frac{x'^2+\gamma^2y'^2}{2\sigma^2}\right) cos\left(2\pi\frac{x'}{\lambda}+\varphi\right). \tag{7}$$

$$g^I_{\lambda,\theta,\varphi,\sigma,\gamma}(x,y) = exp\left(-\frac{x'^2+\gamma^2y'^2}{2\sigma^2}\right) sin\left(2\pi\frac{x'}{\lambda}+\varphi\right). \tag{8}$$

where $x' = x\ \cos\theta + y sin\boldsymbol{\theta}$; $y' = -\ x\ cos\boldsymbol{\theta} + y cos\boldsymbol{\theta}$; λ represents wavelength of sine function, θ denotes the orientation of the Gabor function relative to the parallel bands, $\sigma\varphi$ represents offset's phase, γ and σ designate spatial aspect ratio and Gaussian function scale respectively. Green channel image I_g is convolved with Gabor filter $g(x,y)$ to provide Gabor filter response $G(x,y)$, given by the following equation:

$$G(x,y) = g(x,y)*I_g(x,y). \tag{9}$$

where * designates convolution operator. In this article, we computed maximum Gabor filter answer over the range from 0 to π in increments of π/16 radians, for each pixel at distinct scales [2,4,6,8]. Each image's pixel is computed for each scale using different frequencies [0.1,1.0] with maximum response, taken as a feature. Thus, Gabor responses are generated for each image's pixel and are employed for GLM learning method.

3.3.2. Generalized linear models

GLMs are supple variant of linear regression based on various stochastic information generation, allowing them to establish a potentially nonlinear link between the response variable and the explanatory variables of linear model. GLMs used for continuous responses are essentially ordinary regression models. GLMs are superficial learning approach, which just use few part of images for training and test. GLMs primarily have three components: the *random component,* the *systematic component* and the *parametric link function* [45,47].

Random component describes the response variable Y_0 and specifies its probability distribution p. Let x be the intensity of the pixel, ∅ the scale or dispersion parameter, and θ the natural parameter. The corresponding logarithm of likelihood is given by Grégory et al. [47]:

$$\log p(Y_0|x,\theta) := \frac{Y_0(x)\theta(x) - g(\theta(x))}{f(x,\varnothing)} + k(Y_0(x),\ \varnothing\ ). \tag{10}$$

where f is a positive function known as the *dispersion function*, the function $exp(k)$ is referred to as reference measure and is not reliant of the parameters, and g/f is cumulant generating function, also known as the log-partition function of probability density function. We modify the GLM by using the logit link function, also known as the logit model. This differs from the GLM model employed by Grégory et al. [47], where the natural parameter θ plays a less significant role. In our approach, the natural parameter θ is defined as $\log\left|\frac{\pi}{1-\pi}\right|$. The *systematic component* reflects the accuracy of the model's explanatory variables and can be represented as a linear function of β by the linear predictor η, as follows:

$$\eta(x,\beta) := M^T(x)\beta. \tag{11}$$

where M is known as the *design matrix* and β represents the *parameter vector*.

The *link function* g provides an expected average value of the monotonic and smooth mapping. It describes the non-linear relationship between mean value μ of probability density function of the explanatory variables and linear predictor as $g(\mu(x,\beta)) = \eta(x,\beta)$.

Using a simple identity link function g(μ) = μ, as inspired by Agresti et al. [45], we obtain a special case of GLM which consider a standard distribution for Y_0 and directly model its mean.

Let G denote the features extracted from Gabor transform. The learning model *h, as* defined by Fang et al. [32], is given by:

$$h_\theta(G) = \frac{1}{1 + e^{-\theta^T G}} \tag{12}$$

First, the Gabor wavelet transform is used to extract the feature G from retinal vessel image. Testing is performed on one half of the dataset, while the other half is used for training. Lastly, the learning model h receives the extracted features as input. The manually segmented image is used only once for GLM training to learn the feature array for vessel pixel contrast enhancement and background pixel removal.

3.4. Post-processing

The final result of segmentation using supervised GLM is achieved by applying an optimal threshold, determined by maximum Youden's index [48]. This threshold corresponds relatively to the best sensitivity and specificity, which is obtained by performing several Gabor transformations with variable parameters detailed in the previous subsection. After the blood vessel extraction, the segmented image may contain isolated or unwanted pixels, which are removed through a morphological cleaning operation. The morphological operation employed is based on the Match Filter (MF) and the First Derivative Order of Gaussian (FDOG) proposed by Zhang et al. [6]. Parameters such as scale, constant criterion, neighborhood length on the Y axis, threshold, and the number of MF-FDOG orientations were set to values 1, 2.3, 8, 30 and 12 respectively for all images processed during this final operation.

3.5. Result evaluation metrics

Statistical parameters such as sensitivity (Se), specificity (Sp), Dice coefficient, False Discovery Rate (FDR), Positive Predictive Value (PPV), Negative Predictive Value (NPV), Jaccard index, Matthew's Correlation Coefficient (MCC), G-Mean, and Accuracy (Acc) are used to assess the performance of this model. For each tested image, its manually segmented equivalent from the corresponding database is used as a reference, or ground truth. True positives (TP) are pixels identified as blood vessels in both the ground thruth and segmented image; true negatives (TN) are pixels that are identified as non-vessels in both the reference and segmented image; false negatives (FN) are pixels that are identified as non-vessels in the segmented image but as vessels in the reference; and false positives (FP) are the ones pixels that are marked as vessels in the segmented image but not as a vessel in the references.

The ratio of correctly classified vessel pixels to all vessel pixels in the groundtruth image is given by sensitivity (Se). The ratio of the total number of correctly classified non-vessel pixels to the total number of non-vesel pixels is known as specificity (Sp). The harmonic mean of Se and Acc is called the Dice coefficient. The percentage of pixels correctly classified as vessel pixels out of actual vessel pixels is known as the PPV. The ratio of correctly identified non-vessel pixels to all classified non-vessel pixels is determined by Negative Predictive Value (NPV). The False Discovery Rate (FDR) represents the proportion of false positives among all positive classifications. Matthew's Correlation Coefficient (MCC) quantifies the quality of binary classifications. The Jaccard index measures the ratio of the intersection of true positives and true negatives to the union of these sets. Finally, the ratio of correctly identified pixels to the total number of pixels in the image represents accuracy (Acc). Table 1 provides the mathematical expressions for these parameters [49–60].

We also assessed another metric of our model's performance using ROC (Receiver Operating Characteristic) curve. As a reminder, this curve represents True Positive Rate (TPR) compared to False Positive Rate (FPR) for various obtained thresholds. We then computed Area Under the ROC Curves (AUC) to compare performance of image segmentation. Higher the value of the AUC, the better the quality of segmentation [51–56].

4. Experimental results and analysis

Fig. 2 shows the results of main processing phases of proposed approach for an image sample using the DRIVE database.
Figs. 3–5 show the vessel segmentation results of the proposed algorithm for a several randomly selected images from the DRIVE,

Table 1
Performance measerements for retinal vessel segmentation.

Measures	Equation
Se	TP/(TP + FN)
Sp	TN/(TN + FP)
Dice coefficient	2TP/(2 TP + FP + FN)
PPV	TP/(TP + FP)
NPV	TN/(TN + FN)
FDR	FP/(FP + TN)
Jaccard Index	TP/(TP + FP + FN)
MCC	(TP x TN – FP x FN)/ $\sqrt{(TP+FP)(TP+FN)(TN+FP)(TN+FN)}$
G-Mean	$\sqrt{\text{Se x Sp}}$
Acc	**Acc = (TP + TN)/(TP + FP + TN + FN)**

STARE and CHASE_DB1 databases, respectively. The original images are displayed in the first row, the results of the manual segmentation provided by an expert and used as a ground truth are shown in the second row, and the images of the detected vessels using the suggested method are shown in the third row.

The results of various performance metrics computed for the DRIVE, STARE and CHASE_DB1 databases are presented in Tables 2–4, respectively. The mathematical formulas provided in Table 1 are used to calculate the performance measures for each image from the three databases used.

The average performance metrics of the proposed model are as follows: for the DRIVE database, the model achieved an accuracy (Acc) of 0.9643, sensitivity (Se) of 0.7998, and specificity (Sp) of 0.9792. For the STARE database, the model's accuracy was 0.9553, sensitivity was 0.7059, and specificity was 0.9776. For the CHASE_DB1 database, the accuracy was 0.9593, sensitivity was 0.7225, and specificity was 0.9786. The ROC curves for our method are shown in Figs. 6–8. The AUC values of 0.9767 for DRIVE, 0.9682 for STARE, and 0.9722 for CHASE_DB1 are obtained.

Figs. 9–11 display the impact of the FDCT during the preprocessing phase. We observed a significant improvement in average accuracies with the inclusion of FDCT in the preprocessing step.

We compared the obtained performances with those of existing methods. The comparison results are presented in Tables 5–7 for DRIVE, STARE and CHASE_DB1 databases, respectively. For this purpose, the models proposed by Tavakoli et al. [3], Dash and Bhoi [8], Ravichandran et al. [10], Saleh et al. [12], Zhang et al. [18], Soares et al. [28], Guo et al. [31], Fang et al. [32], Geethalakshmi et al. [35], Feudjio et al. [38], Jadoon et al. [49], Khomri et al. [50], Saha et al. [51], Hu et al. [52], Yan et al. [53], Zhang et al. [54], Azzopardi et al. [55], Kejuan et al. [56], Zhao et al. [57], Fraz et al. [58], Nayab et al. [59], Fraz et al. [60], Vega et al. [61], Aslani et al. [62], Mapayi et al. [63], Farokhain et al. [64], Mendonca et al. [65], You et al. [66], Lam et al. [67], Marin et al. [68], Lin et al. [69], Alhussein et al. [71], Dash et al. [72], Dash et al. [73], Soomro et al. [74], Dash et al. [75] are used. The results of authors Vega et al. [61], Aslani et al. [62], Mapayi et al. [63] and Farokhian et al. [64] are obtained from Dash and Bhoi [8]. Those of the authors Mendonca et al. [65], You et al. [66], Lam et al. [67], Marin et al. [68] and Lin et al. [69] are obtained from Saha et al. [51]. The remaining values were sourced directly from the original literature. The symbol "/" denotes values that are not provided in the original study.

We observe that the average accuracy of 0.9643 achieved by the proposed model on the DRIVE database images exceeds the performance of the thirteen supervised methods listed in Table 5. Among the twenty-one unsupervised segmentation techniques in the same table, our model ranks among the top five performances. Additionally, the average AUC value of 0.9767 places it as the third-best performance among the thirty-four methods reviewed for the DRIVE dataset.

Furthermore, Table 6 shows that the average accuracy of 0.9553 achieved on the STARE database images exceeds that of several segmentation methods, including unsupervised approach using morphological operators and curvelets proposed by Feudjio et al. [38],

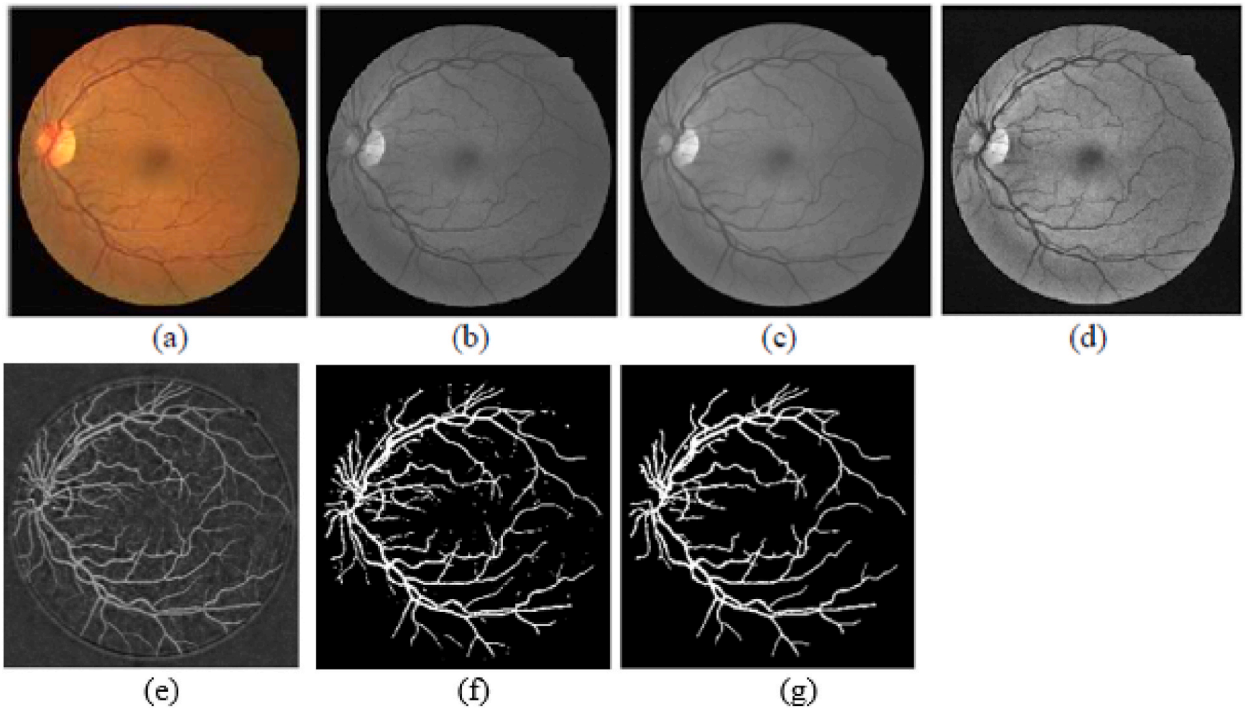

Fig. 2. Visual inspection of the processing steps of the proposed system using the DRIVE database: (a) original image, (b) green channel, (c) FDCT enhanced, (d) CLAHE enhanced, (e) Output GLM, (f) Post-processing operation, (g) Final image. (For interpretation of the references to color in this figure legend, the reader is referred to the Web version of this article.)

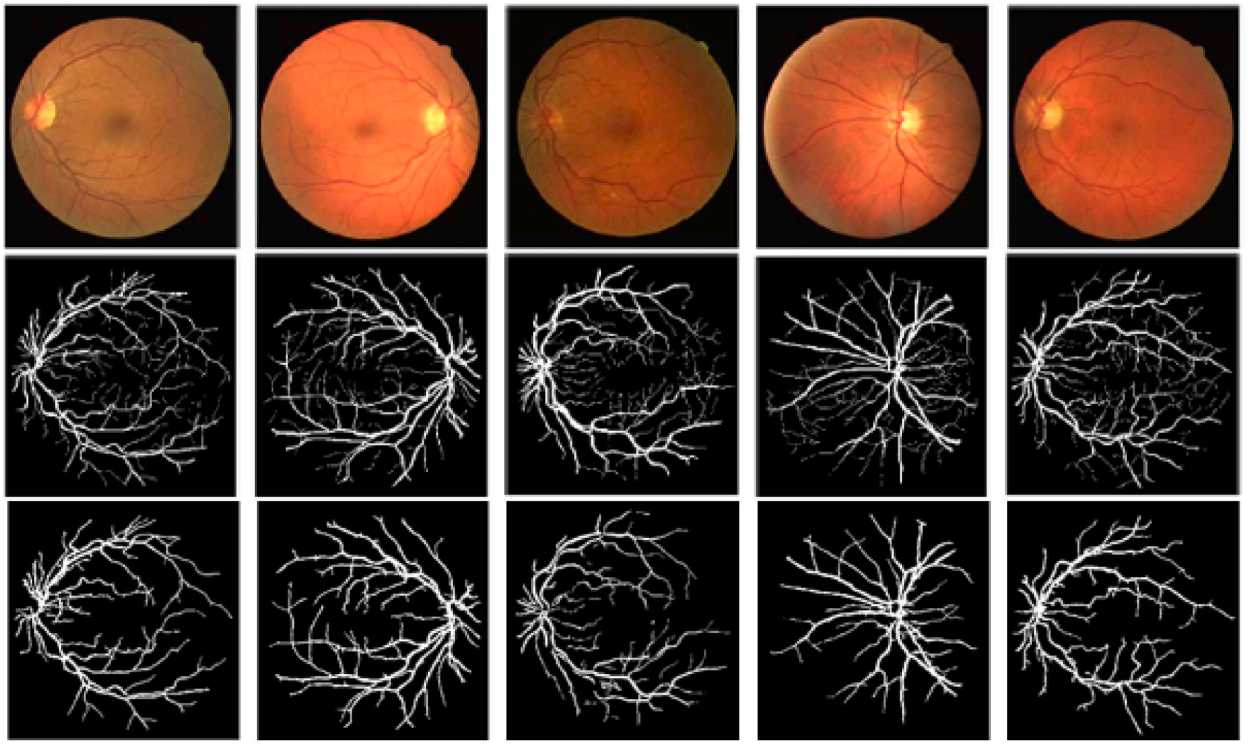

Fig. 3. Blood vessel extraction results on DRIVE database. First row: original images. Second row: ground truth images (same order as first row). Third row: segmentation results from the proposed method (same order as first row).

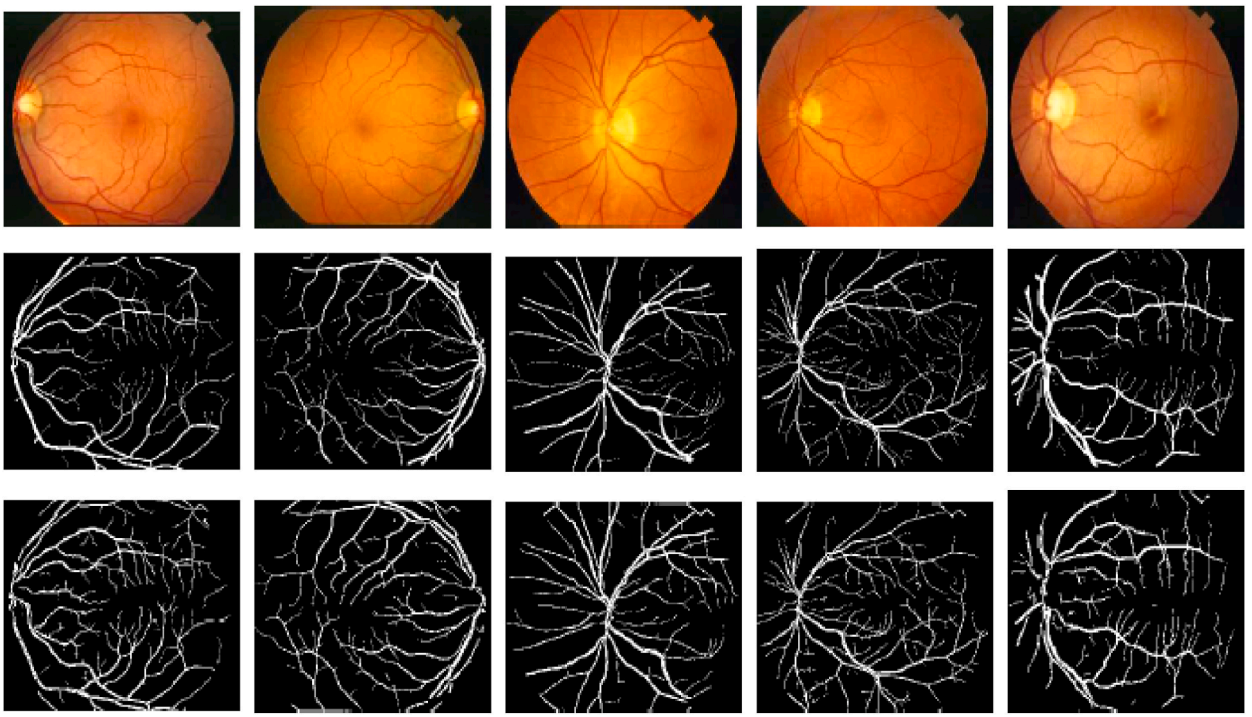

Fig. 4. Blood vessel extraction results on STARE database. First row: original images; Second row: ground truth images (same order as first row); Third row: segmentation results from the proposed method (same order as first row).

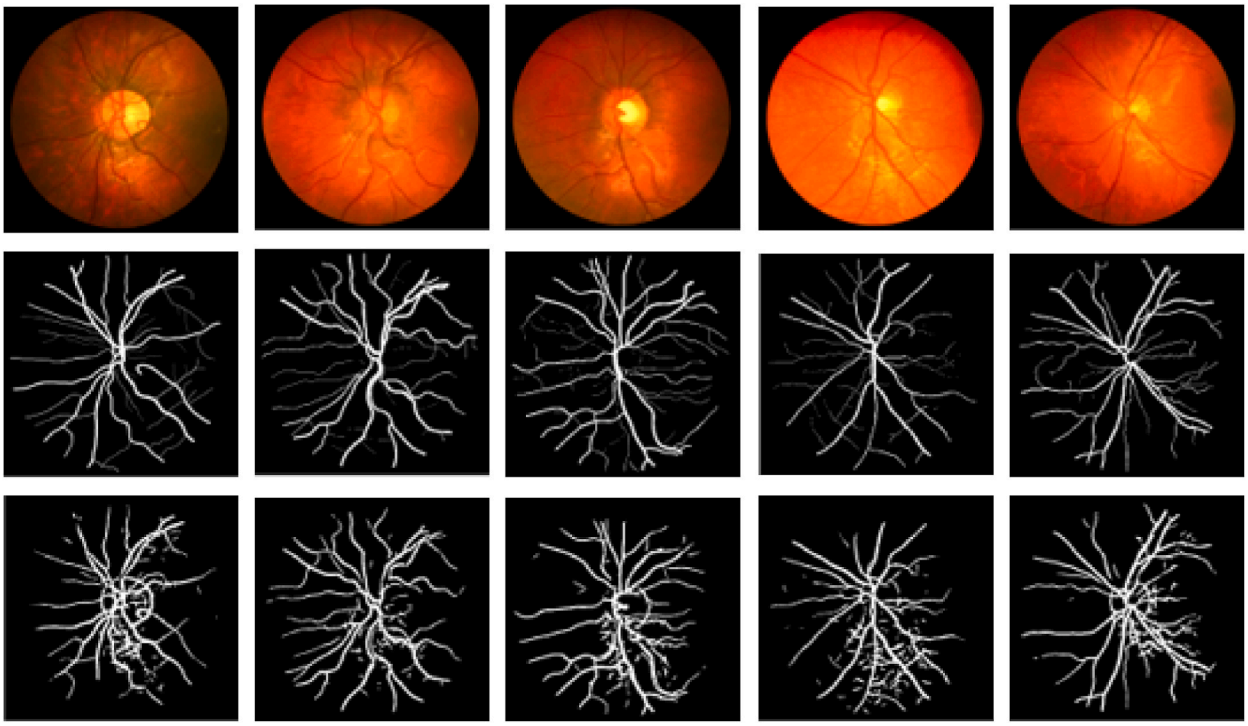

Fig. 5. Blood vessel extraction results on CHASE_DB1 database. First row: original images; Second row: ground truth images (same order as first row); Third row: segmentation results from the proposed method (same order as first row).

Table 2
Performance metrics on DRIVE database.

Image	Se	Sp	Dice Coefficient	PPV	NPV	FDR	**Jaccard index**	MCC	G-Mean	Acc	AUC
01_test	0.8497	0.9734	0.7988	0.7536	0.9854	0.0266	0.6649	0.7799	0.9095	0.9626	0.9792
02_test	0.8690	0.9774	0.8392	0.8114	0.9852	0.0226	0.7229	0.8211	0.9216	0.9664	0.9838
03_test	0.7968	0.9796	0.7944	0.7921	0.9801	0.0204	0.6590	0.7743	0.8835	0.9633	0.9775
04_test	0.7910	0.9817	0.7981	0.8054	0.9800	0.0183	0.6641	0.7790	0.8812	0.9649	0.9705
05_test	0.8443	0.9803	0.8171	0.7916	0.9861	0.0197	0.6908	0.8009	0.9098	0.9693	0.9811
06_test	0.7541	0.9790	0.7701	0.7868	0.9749	0.0210	0.6262	0.7473	0.8593	0.9581	0.9665
07_test	0.8013	0.9821	0.7879	0.7750	0.9846	0.0179	0.6500	0.7714	0.8871	0.9691	0.9699
08_test	0.7356	0.9818	0.7393	0.7431	0.9811	0.0182	0.5864	0.7208	0.8498	0.9654	0.9682
09_test	0.7418	0.9792	0.7498	0.7580	0.9774	0.0208	0.5998	0.7282	0.8523	0.9600	0.9628
10_test	0.8215	0.9806	0.7930	0.7664	0.9861	0.0194	0.6570	0.7769	0.8976	0.9692	0.9785
11_test	0.8025	0.9808	0.7969	0.7914	0.9821	0.0192	0.6624	0.7784	0.8872	0.9660	0.9713
12_test	0.8047	0.9787	0.7855	0.7673	0.9829	0.0213	0.6468	0.7666	0.8874	0.9647	0.9784
13_test	0.7766	0.9745	0.7754	0.7741	0.9748	0.0255	0.6331	0.7500	0.8700	0.9545	0.9715
14_test	0.8061	0.9814	0.7918	0.7779	0.9843	0.0186	0.6553	0.7748	0.8895	0.9683	0.9800
15_test	0.7596	0.9833	0.7724	0.7855	0.9807	0.0167	0.6292	0.7545	0.8642	0.9666	0.9710
16_test	0.8341	0.9783	0.8068	0.7813	0.9845	0.0217	0.6762	0.7887	0.9033	0.9660	0.9788
17_test	0.7656	0.9819	0.7686	0.7715	0.9813	0.0181	0.6241	0.7502	0.8670	0.9659	0.9768
18_test	0.8324	0.9782	0.8130	0.7944	0.9830	0.0218	0.6849	0.7938	0.9024	0.9648	0.9759
19_test	0.8317	0.9774	0.8165	0.8018	0.9814	0.0226	0.6899	0.7960	0.9016	0.9629	0.9767
20_test	0.7765	0.9754	0.7696	0.7628	0.9771	0.0246	0.6255	0.7459	0.8703	0.9569	0.9665
Average	**0.7998**	**0.9792**	**0.7892**	**0.7796**	**0.9816**	**0.0208**	**0.6524**	**0.7699**	**0.8847**	**0.9643**	**0.9767**

and the supervised technique combining classical filters with neural networks proposed by Saha et al. [51]. Notably, the average accuracy of 0.9593 achieved on the CHASE_DB1 dataset is the second-best performance among the unsupervised methods listed in Table 7. This performance also surpasses that of the supervised methods proposed by Saha et al. [51], Fraz et al. [60], and Lin et al. [69], as shown in the same table. Additionally, the average AUC of 0.9722 achieved on this dataset is the second-best performance among all approaches listed in the table, just after the deep learning-based joint loss segmentation model proposed by Yan et al. [53].

To further assess the effectiveness of our algorithm, the qualitative result of the segmentation of image named *01_test* of the DRIVE database is compared to that of few literature models. This graphical comparison, which includes results from Tavakoli et al. [3], Dash and Bhoi [8], Ravichandran et al. [10], Saleh et al. [12], Zhang et al. [18], Fang et al. [32], Zhao et al. [57], Fraz et al. [58] and Mapayi

Table 3
Performance metrics on STARE database.

Image	Se	Sp	Dice Coefficient	PPV	NPV	FDR	**Jaccard index**	MCC	G-Mean	Acc	AUC
im0001	0.5317	0.9591	0.5254	0.5193	0.9621	0.0441	0.3557	0.4835	0.7144	0.9369	0.9536
im0002	0.6987	0.9614	0.4828	0.4678	0.9669	0.0418	0.3177	0.4446	0.6926	0.9325	0.9462
im0003	0.6179	0.9708	0.5869	0.5588	0.9784	0.0324	0.4144	0.5598	0.7748	0.9516	0.9653
im0004	0.6143	0.9873	0.419	0.6301	0.9501	0.0159	0.2648	0.4155	0.5568	0.9393	0.9538
im0005	0.6589	0.973	0.6762	0.6945	0.9691	0.0302	0.5095	0.645	0.8011	0.9466	0.9613
im0044	0.8041	0.97	0.7213	0.6541	0.9879	0.0332	0.5626	0.7023	0.8836	0.9603	0.9749
im0077	0.8365	0.9746	0.7788	0.7287	0.9884	0.0286	0.6359	0.76	0.9034	0.9655	0.9792
im0081	0.7936	0.9764	0.6906	0.6875	0.9781	0.0268	0.526	0.6652	0.8233	0.9572	0.9709
im0082	0.771	0.9808	0.7644	0.7579	0.9833	0.0224	0.6168	0.7439	0.87	0.9662	0.9789
im0139	0.7258	0.9743	0.7116	0.6979	0.9788	0.0289	0.5508	0.6857	0.8414	0.9563	0.9727
im0162	0.8337	0.9816	0.795	0.7598	0.99	0.0216	0.6577	0.7793	0.9051	0.973	0.9857
im0163	0.8649	0.9791	0.81	0.7616	0.9914	0.0241	0.6785	0.7946	0.9207	0.9722	0.9849
im0235	0.7199	0.986	0.7648	0.8158	0.9757	0.0172	0.6174	0.7449	0.8429	0.9642	0.9779
im0236	0.7048	0.9877	0.7633	0.8323	0.9738	0.0155	0.6153	0.7446	0.8347	0.964	0.9757
im0239	0.5913	0.9785	0.6432	0.7052	0.9648	0.0247	0.4729	0.6153	0.7609	0.947	0.9607
im0240	0.6106	0.9799	0.5991	0.725	0.9489	0.0233	0.4267	0.5723	0.7075	0.9338	0.9475
im0255	0.7829	0.9859	0.8053	0.829	0.9816	0.0173	0.6719	0.7869	0.879	0.9697	0.9714
im0291	0.656	0.9831	0.582	0.6106	0.9794	0.0201	0.4096	0.5614	0.7396	0.9634	0.9771
im0319	0.5741	0.981	0.5629	0.5522	0.9837	0.0222	0.3909	0.5428	0.7507	0.9654	0.9781
im0324	0.6359	0.9816	0.4142	0.5408	0.9567	0.0216	0.2609	0.3948	0.574	0.9405	0.9552
Average	**0.7059**	**0.9776**	**0.6548**	**0.6764**	**0.9745**	**0.0256**	**0.4978**	**0.6321**	**0.7888**	**0.9553**	**0.9682**

Table 4
Performance metrics on CHASE_DB1 database.

Image	Se	Sp	Dice Coefficient	PPV	NPV	FDR	**Jaccard index**	MCC	G-Mean	Acc	AUC
01L	0.6907	0.9751	0.6751	0.7042	0.9739	0.0275	0.5385	0.6413	0.7864	0.9536	0.9659
02L	0.6994	0.9491	0.6031	0.5988	0.9706	0.0353	0.4663	0.5596	0.7659	0.9477	0.9596
03L	0.6385	0.9913	0.6906	0.7616	0.9716	0.0226	0.5546	0.6534	0.7684	0.9659	0.9783
04L	0.7632	0.9917	0.6242	0.7089	0.9646	0.0225	0.487	0.5728	0.716	0.9595	0.9728
05L	0.7961	1.0059	0.84	0.9816	0.9738	0.0182	0.7221	0.8135	0.8211	0.9721	0.9857
06L	0.6917	0.9674	0.644	0.6572	0.9736	0.0298	0.5067	0.609	0.7793	0.9464	0.9586
07L	0.7784	0.9915	0.73	0.798	0.9747	0.0226	0.5966	0.6997	0.7951	0.9691	0.9826
08L	0.7254	0.9693	0.6295	0.6153	0.9817	0.0292	0.4923	0.6167	0.8029	0.9543	0.9666
09L	0.7241	0.998	0.6824	0.6815	0.9892	0.0206	0.546	0.6903	0.831	0.9768	0.9895
10L	0.6359	0.9801	0.5895	0.5975	0.9773	0.026	0.4532	0.5625	0.7552	0.9598	0.9731
11L	0.7741	0.9791	0.65	0.6185	0.9898	0.0263	0.5128	0.6644	0.843	0.9713	0.9825
12L	0.7154	0.9738	0.6819	0.6994	0.977	0.0279	0.5455	0.6555	0.8011	0.9551	0.9674
13L	0.7455	0.9768	0.6405	0.6385	0.9811	0.027	0.5032	0.6253	0.7978	0.9607	0.9783
14L	0.7363	0.9506	0.5495	0.5068	0.983	0.0348	0.4154	0.5433	0.791	0.9378	0.9498
Average	**0.7225**	**0.9786**	**0.6593**	**0.6834**	**0.9773**	**0.0265**	**0.5243**	**0.6362**	**0.7896**	**0.9593**	**0.9722**

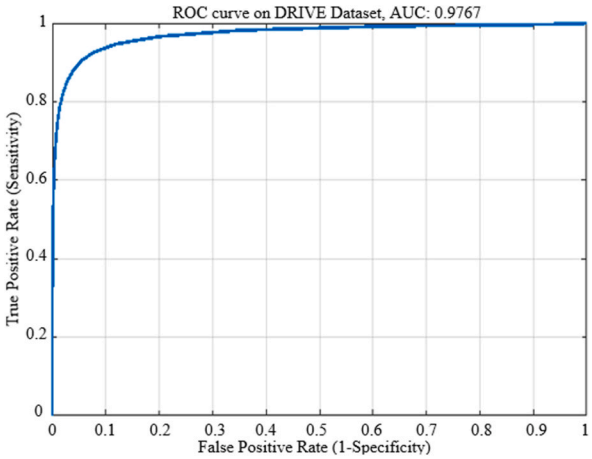

Fig. 6. ROC curve on drive dataset.

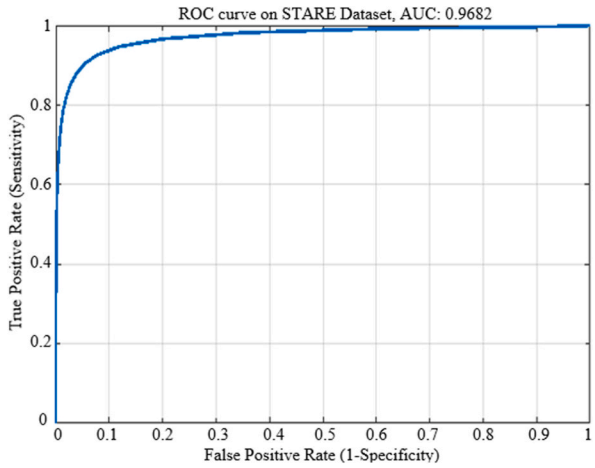

Fig. 7. ROC curve on stare dataset.

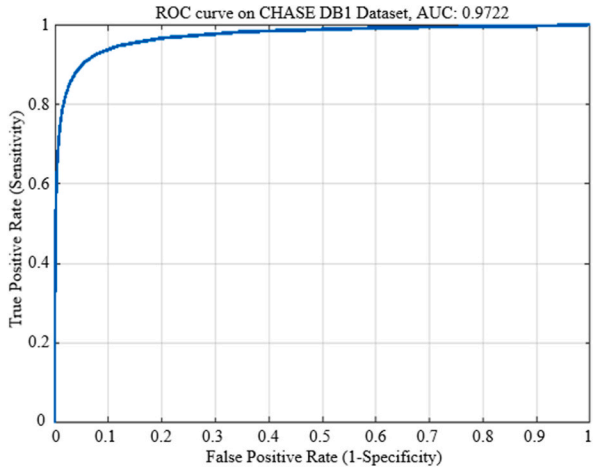

Fig. 8. ROC curve on CHASE_DB1 dataset.

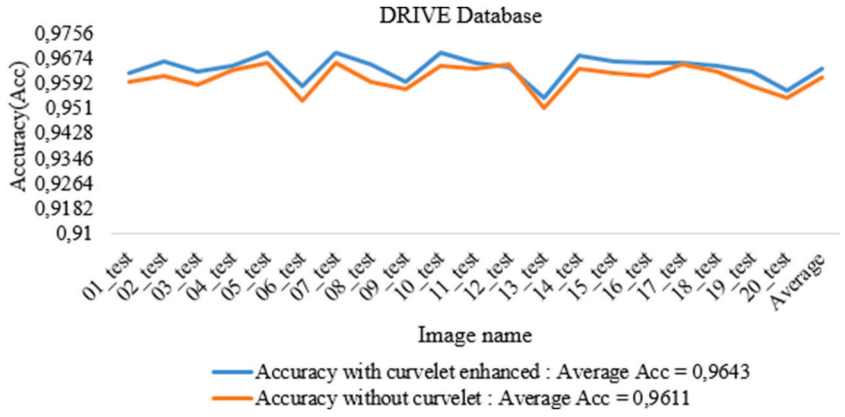

Fig. 9. Average accuracies obtained using or not curvelet transforms during the preprocessing stage on DRIVE database.

et al. [63], is presented in Fig. 12.

We examined key details in a representative image from several state-of-the-art algorithms to assess the reliability of the proposed approach, as illustrated in Fig. 13. Fig. 13 (e) and (g) show that our model more effectively removes isolated or unwanted segments

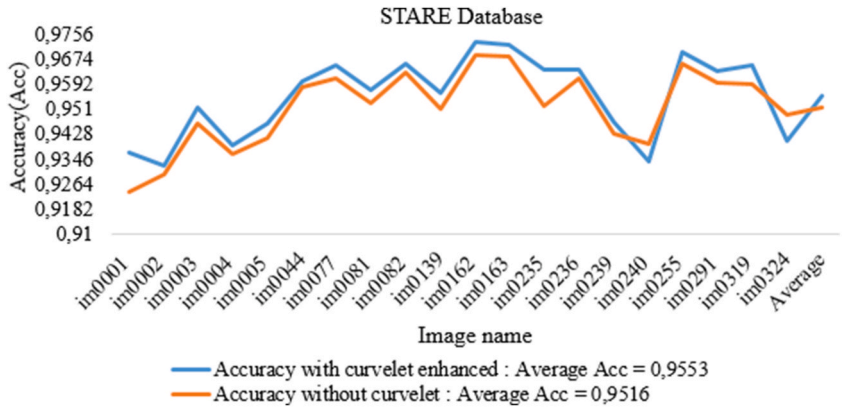

Fig. 10. Average accuracies obtained using or not curvelet transforms during the preprocessing stage on STARE database.

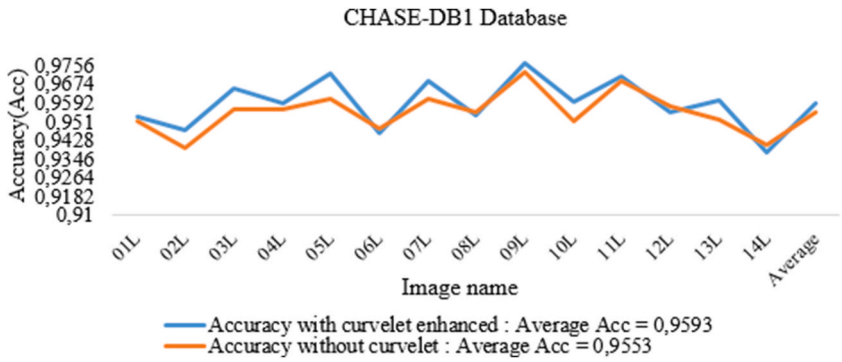

Fig. 11. Average accuracies obtained using or not curvelet transforms during the preprocessing stage on CHASE_DB1 database.

compared to techniques using CLAHE combined with gamma correction, as proposed by Dash and Bhoi [8]. The same improvement is observed in Fig. 13 (g) when compared to the segmentation approach based on GLCM energy information proposed by Mapayi et al. [63]. Additionally, Fig. 13 (f) highlights the model's capability to detect segments that were missed by the automatic threshold selection method proposed by Saleh et al. [12].

Clinical signs of certain pathologies, such as diabetic retinopathy, include, among others, spots in the area of retinal vessels, hemorrhagic points, cotton wool spots, or hard exudates [20]. The ability of our model to detect vessels with continuity and to eliminate isolated or undesirable points in regions illustrated by Fig. 13, for example, may help reduce the rate of false positives in the diagnosis of these types of ocular conditions.

5. Conclusion

We have presented a new automated and semi-supervised algorithm for extracting blood vessels from retinal images. The approach is primarily a hybrid segmentation method that leverages the strengths of both supervised and unsupervised techniques while mitigating their respective limitations. The initial key step involved optimizing the widely used CLAHE technique by incorporating a digital implementation of FDCT during the preprocessing phase of retinal background images. Another distinctive feature of our approach is the use of a supervised intermediate step with a GLM learning model, utilizing the identity link function. This model was specifically employed for training and testing on a subset of image features extracted using Gabor filters. For the final binarization, the optimal threshold was determined automatically by maximizing the Youden index. A morphological cleaning operation, utilizing the MF-FDOG operator with fixed parameters, effectively removed isolated or unwanted segments that remained after the unsupervised process. The experimental results presented average accuracies of 0.9553, 0.9643 and 0.9593, with corresponding AUC values of 0.9682, 0.9767 and 0.9722 for the STARE, DRIVE and CHASE_DB1 databases, respectively. Based on comparative studies conducted, these results indicate that the proposed model demonstrates statistically acceptable performance compared to other known algorithms in the literature. Moreover, the proposed algorithm is based on straightforward processing techniques that are well-regarded for their ease of implementation. This approach is highly suitable for automated processing and enhances the optimization of diagnostic tools for various retinal disorders.

Table 5
Performance of the suggested model compared to other studies based on DRIVE.

Types	Methods	Se	Sp	Acc	AUC
Supervised methods	Zhang et al. [18]	0.7861	0.9712	0.9466	0.9703
	Soares et al. [28]	/	/	0.9466	0.9614
	Guo et al. [31]	0.7729	0.9826	0.9640	/
	Saha et al. [51]	0.7352	0.9775	0.9480	0.9678
	Hu et al. [52]	0.7772	0.9793	0.9533	0.9759
	Yan et al. [53]	0.7653	0.9818	0.9542	0.9752
	Kejuan et al. [56]	0.8199	0.9762	0.9561	0.9796
	Fraz et al. [60]	0.7406	0.9807	0.9480	0.9747
	Vega et al. [61]	0.744	0.960	0.941	/
	Aslani et al. [62]	0.754	0.980	0.951	/
	Mendonca et al. [65]	0.7344	0.9764	0.9452	/
	Lam et al. [67]	0.7067	0.9801	0.9452	/
	Lin et al. [69]	0.7632	/	0.9536	/
Unsupervised methods	Tavakoli et al. [3]	/	/	0.9688	0.9739
	Dash and Bhoi [8]	0.7417	0.9861	0.9571	/
	Ravichandran et al. [10]	0.7259	0.9799	0.9574	/
	Muzammil et al. [11]	0.7271	0.9798	0.9573	/
	Saleh et al. [12]	0.8423	/	0.9630	/
	Fang et al. [32]	/	/	0.96	/
	Geethalakshmi et al. [35]	0.755	0.989	0.965	/
	Feudjio et al. [38]	0.7406	0.9878	0.9667	/
	Khomri et al. [50]	0.7390	0.9740	0.9450	/
	Zhang et al. [54]	0.7743	0.9725	0.9476	0.9636
	Azzopardi et al. [55]	0.7655	0.9704	0.9442	0.9614
	Zhao et al. [57]	0.7354	0.9789	0.9477	/
	Fraz et al. [58]	0.7302	0.9742	0.9422	/
	Nayab et al. [59]	0.7271	0.9798	0.9573	/
	Mapayi et al. [63]	0.731	0.972	0.951	/
	Farokhain et al. [64]	0.6933	0.9777	0.9392	0.9530
	Alhussein et al. [71]	0.7855	0.9734	0.9559	0.8787
	Dash et al. [72]	0.6907	0.9904	0.964	/
	Dash et al. [73]	0.7403	0.9905	0.9661	/
	Soomro et al. [74]	0.812	0.971	0.963	/
	Dash et al. [75]	0.7043	0.9890	0.9613	/
	Proposed method	0.7998	0.9792	0.9643	0.9767

Table 6
Performance of the suggested approach compared to other studies on STARE database.

Types	Methods	Se	Sp	Acc	AUC
Supervised methods	Zhang et al. [18]	0.7882	0.9729	0.9547	0.9740
	Saha et al. [51]	0.7265	0.9759	0.9548	0.9686
	Hu et al. [52]	0.7543	0.9814	0.9632	0.9751
	Yan et al. [53]	0.7581	0.9846	0.9612	0.9801
	Fraz et al. [60]	0.7548	0.9763	0.9534	0.9768
	You et al. [66]	0.7260	0.9756	0.9479	/
	Lam et al. [67]	/	/	0.9567	/
	Marin et al. [68]	0.6944	0.9819	0.9526	/
	Lin et al. [69]	0.7423	/	0.9603	/
Unsupervised methods	Tavakoli et al. [3]	/	/	0.9646	0.9701
	Ravichandran et al. [10]	0.7693	0.9672	0.9526	/
	Muzammil et al. [11]	0.7164	0.9760	0.9560	/
	Feudjio et al. [38]	0.7028	0.9755	0.9507	/
	Jadoon et al. [49]	0.7201	0.9708	0.9498	/
	Khomril et al. [50]	0.737	0.962	0.94	/
	Zhang et al. [54]	0.7791	0.9758	0.9554	0.9748
	Azzopardi et al. [55]	0.7716	0.9701	0.9497	0.9563
	Zha et al. [57]	0.7187	0.9767	0.9509	/
	Fraz et al. [58]	0.7318	0.9660	0.9423	/
	Nayab et al. [59]	0.7164	0.9760	0.9560	/
	Mendonca et al. [65]	0.6996	0.9730	0.9440	/
	Soomro et al. [74]	0.809	0.969	0.958	/
	Proposed method	0.7059	0.9776	0.9553	0.9682

Table 7
Performance of the suggested approach compared to other studies on CHASE_DB1 database.

Types	Methods	Se	Sp	Acc	AUC
Supervised methods	Zhang et al. [18]	0.7644	0.9716	0.9602	0.9706
	Saha et al. [51]	0.7279	0.9658	0.9452	0.9681
	Yan et al. [53]	0.7633	0.9809	0.9610	0.9781
	Fraz et al. [60]	0.7224	0.9711	0.9469	0.9712
	Lin et al. [69]	0.7815	/	0.9587	/
Unsupervised methods	Tavakoli et al. [3]	/	/	0.9475	0.9712
	Dash and Bhoi [8]	0.755	0.980	0.952	/
	Zhang et al. [54]	0.7626	0.9661	0.9452	0.9606
	Azzopardi et al. [55]	0.7585	0.9587	0.9387	0.9487
	Alhussein et al. [71]	0.7776	0.9634	0.9505	0.8705
	Dash et al. [75]	0.7153	0.9816	0.9605	/
	Proposed method	0.7225	0.9786	0.9593	0.9722

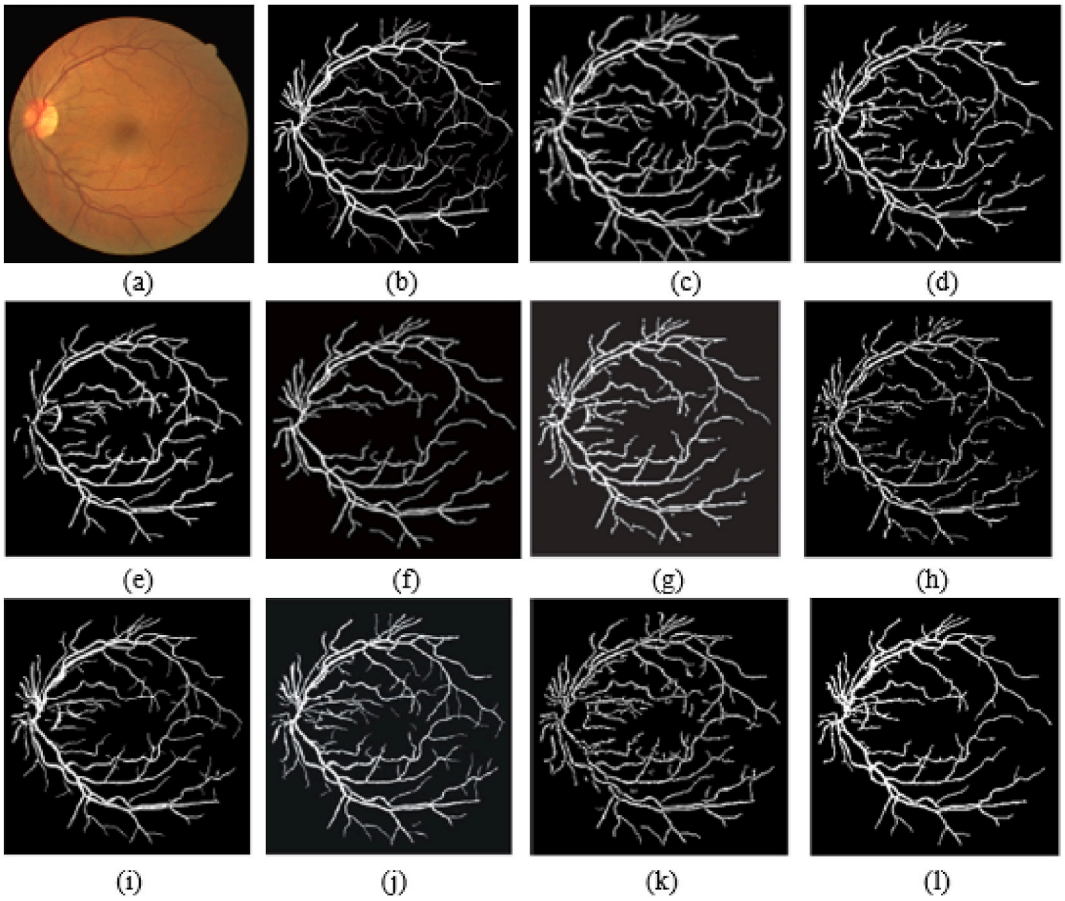

Fig. 12. The obtained results on image named *01_test* of DRIVE database: (a) Original image (b) Ground truth, (c) Tavakoli et al. [3], (d) Dash and Bhoi [8], (e) Ravichandran et al. [10], (f) Saleh et al. [12], (g) Zhang et al. [18], (h) Fang et al. [32], (i) Zhao et al. [57], (j) Fraz et al. [58], (k) Mapayi et al. [63], (l) Proposed model.

Funding

The authors declare that no funds, grants, or other support were received during the preparation of this manuscript.

Ethics approval

This article does not contain any studies with human participants and/or animals performed by any of the authors.

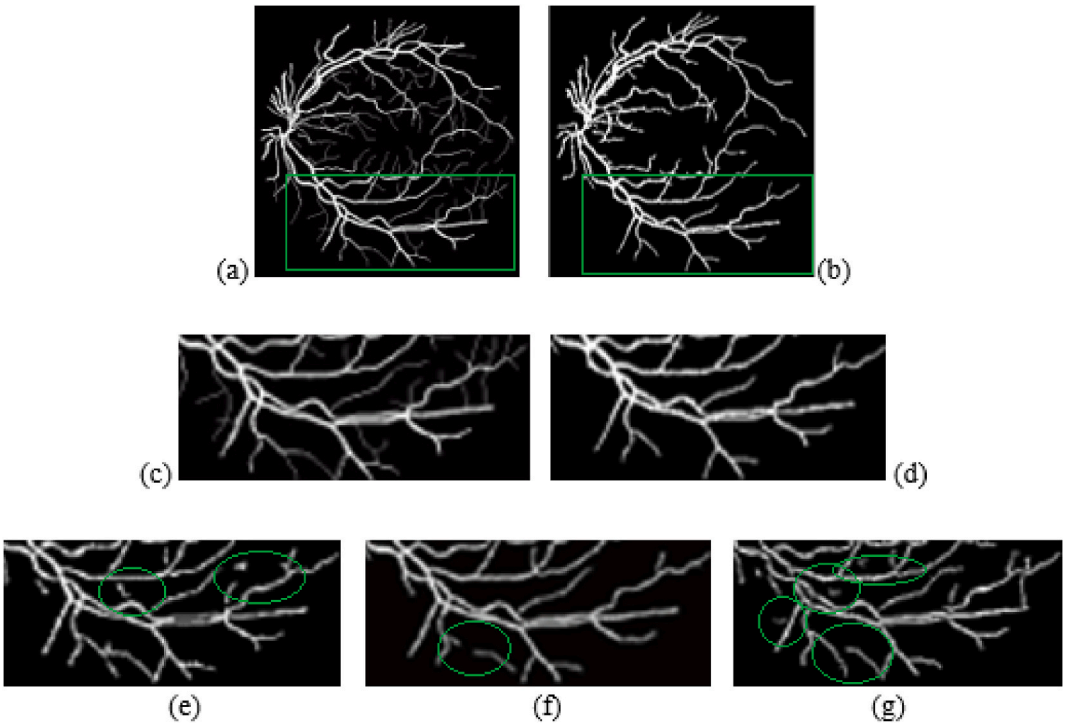

Fig. 13. Detailed comparison of some state-of-art approaches and the suggested algorithm: (a) and (c) Marked sub-region on Ground truth image (b) and (d) Marked sub-region of our obtained result, (e) Dash and Bhoi [8], (f) Saleh et al. [12], (g) Mapayi et al. [63].

Consent to participate

Not applicable.

Consent to publish

Not applicable.

Data availability

Data will be made available on request.

CRediT authorship contribution statement

Feudjio Ghislain: Writing – review & editing, Writing – original draft, Methodology, Investigation, Funding acquisition, Formal analysis, Conceptualization. **Saha Tchinda Beaudelaire:** Writing – review & editing, Validation, Resources, Methodology, Investigation, Funding acquisition, Formal analysis, Conceptualization. **Tchiotsop Daniel:** Validation, Supervision, Project administration, Funding acquisition.

Declaration of competing interest

The authors declare that they have no known competing financial interests or personal relationships that could have appeared to influence the work reported in this paper.

References

[1] R. Imtiaz, T.M. Khan, S.S. Naqvi, M. Arsalan, S.J. Nawaz, Screening of Glaucoma disease from retinal vessel images using semantic segmentation, Comput. Electr. Eng. 91 (2021) 107036, https://doi.org/10.1016/j.compeleceng.2021.107036.
[2] M.T. Islam, S.T. Mashfu, A. Faisal, S.C. Siam, I.T. Naheen, R. Khan, Deep learning-based glaucoma detection with cropped optic cup and disc and blood vessel segmentation, IEEE Access 10 (2021) 2828–2841, https://doi.org/10.1109/ACCESS.2021.3139160.
[3] M. Tavakoli, A. Mehdizadeh, S.R. Pourreza, J. Dehmeshki, Unsupervised automated retinal vessel segmentation based on Radon line detector and morphological reconstruction, IET Image Process. 15 (7) (2021), https://doi.org/10.1049/ipr2.12119, 1484-14.

[4] R. Liu, S. Gao, H. Zhang, S. Wang, L. Zhou, J. Liu, MTNet : a combined diagnosis algorithm of vessel segmentation and diabetic retinopathy for retinal images, PLoS One 17 (11) (2022) e0278126, https://doi.org/10.1371/journal.pone.0278126. Nov 2023.

[5] J.H. Tan, U.R. Acharya, S.V. Bhandary, K.C. Chua, S. Sivaprasad, Segmentation of optic disc, fovea and retinal vasculature using a single convolutional neural network, Journal of Computational Science 20 (2017) 70–79, https://doi.org/10.1016/j.jocs.2017.02.006.

[6] B. Zhang, L. Zhang, L. Zhang, F. Karray, Retinal vessel extraction by matched filter with first-order derivative of Gaussian, Comput. Biol. Med. 40 (4) (2010) 438–445. https://doi:10.1016/j.compbiomed.2010.02.008.

[7] A. Malhi, R. Grewal, H.S. Pannu, Detection and diabetic retinopathy grading using digital retinal images, International Journal of Intelligent Robotics and Applications 7 (2023) 426–458, https://doi.org/10.1007/s41315-022-00269-5.

[8] J. Dash, N. Bhoi, An unsupervised approach for extraction of blood vessels from fundus images, J. Digit. Imag. 31 (2018) 857–868, https://doi.org/10.1007/s10278-018-0059-x.

[9] M. Hashemzadeh, B.A. Azar, Retinal blood vessel extraction employing effective image features and combination of supervised and unsupervised machine learning methods, Artif. Intell. Med. 95 (2019) 1–15, https://doi.org/10.1016/j.artmed.2019.03.001.

[10] C.G. Ravichandran, J.B. Raja, A fast enhancement/thresholding based blood vessel segmentation for retinal image using contrast limited adaptive histogram equalization, J. Med. Imaging Health Inform. 4 (4) (2014) 567–575, https://doi.org/10.1166/jmihi.2014.1289.

[11] N. Muzammil, S.A. Shah, A. Shahzad, M.A. Khan, R.M. Ghoniem, Multifilters-based unsupervised method for retinal blood vessel segmentation, Appl. Sci. 12 (13) (2022) 6393, https://doi.org/10.3390/app12136393.

[12] M.D. Saleh, C. Eswaran, A. Mueen, An automated blood vessel segmentation algorithm using histogram equalization and automatic threshold selection, J. Digit. Imag. 24 (4) (2010) 564–572, https://doi.org/10.1007/s10278-010-9302-9.

[13] N. Memari, A.R. Ramli, M.I.B. Saripan, S. Mashohor, M. Moghbel, Retinal blood vessel segmentation by using matched filtering and fuzzy c-means clustering with integrated level set method for diabetic retinopathy assessment, J. Med. Biol. Eng. 39 (2019) 713–731, https://doi.org/10.1007/s40846-018-0454-2.

[14] K. Asem, A.R. Ramli, S.J. Hashim, Z.M. Noh, Image denoising algorithm using second generation wavelet transformation and principle component analysis, Res. J. Appl. Sci. Eng. Technol. 8 (3) (2014) 367–377.

[15] Z. Zhen, S. Ma, H. Liu, Y. Gong, An edge detection approach based on directional wavelet transform, Comput. Math. Appl. 57 (8) (2009) 1265–1271, https://doi.org/10.1016/j.camwa.2008.11.013.

[16] S. Dash, S. Verma, Kavita, M.S. Khan, M. Wozniak, J. Shafi, M.F. Ijaz, A hybrid method to enhance thick and thin vessels for blood vessel segmentation, Diagnostics 11 (11) (2021) 2017, https://doi.org/10.3390/diagnostics11112017.

[17] P. Bankhead, C.N. Scholfield, J.G. McGeown, T.M. Curtis, Fast retinal vessel detection and measurement using wavelets and edge location refinement, PLoS One 7 (3) (2012), https://doi.org/10.1371/journal.pone.0032435.

[18] J. Zhang, Y. Chen, E. Bekkers, M. Wang, B. Dashtbozorg, ter Haar Romeny B.M., Retinal vessel delineation using a brain-inspired wavelet transform and random forest, Pattern Recogn. 69 (2017) 107–123, https://doi.org/10.1016/j.patcog.2017.04.008.

[19] K.S. Sil, S.P. Maity, Extraction of retinal blood vessel using curvelet transform and fuzzy c-means, in: 2014 22nd International Conference on Pattern Recognition, IEEE, 2014, https://doi.org/10.1109/ICPR.2014.584.

[20] N. Salamat, M.M. Missen, A. Rashid, Diabetic retinopathy techniques in retinal images: a review, Artif. Intell. Med. 97 (2019) 168–188, https://doi.org/10.1016/j.artmed.2018.10.009.

[21] Z. Gu, J. Cheng, H. Fu, K. Zhou, H. Hao, Y. Zhao, T. Zhang, S. Gao, J. Liu, Ce-net: context encoder network for 2D medical image segmentation, IEEE Trans. Med. Imag. 38 (10) (2019) 2281–2292, https://doi.org/10.1109/TMI.2019.2903562.

[22] M. Krithika alias AnbuDevi, K. Suganthi, Review of semantic segmentation of medical images using modified architectures of UNET, Diagnostics 12 (12) (2022) 3064, https://doi.org/10.3390/diagnostics12123064.

[23] X. Yin, L. Sun, Y. Fu, R. Lu, Y. Zhang, U-Net-Based medical image segmentation, Journal of Healthcare Engineering 2022 (2022), https://doi.org/10.1155/2023/9890389.

[24] S.T. Ahmed, A.J. Afifi, L. Zheng, S. Soomro, J. Gao, H. Olaf, P. Manoranjan, Deep learning models for retinal blood vessels segmentation: a review, IEEE Access 7 (2019) 71696–71717, https://doi.org/10.1109/ACCESS.2019.2920616.

[25] C. Chen, J.H. Chuah, R. Ali, Y. Wang, Retinal vessel segmentation using deep learning: a review, IEEE Access 9 (2021) 111985–112004, https://doi.org/10.1109/ACCESS.2021.3102176.

[26] M.V. Ramana, E.S. Reddy, C. Satayanarayana, Enhanced curvlet transform based artificial neural network for brain tumor diagnosis, Int. J. Eng. Adv. Technol. (2018), https://doi.org/10.1109/ACCESS.2021.3102176.

[27] M.E. Gegundez-Arias, D. Marin-Santos, I. Perez-Borrero, M.J. Vasallo-Vazquez, A new deep learning method for blood vessel segmentation in retinal images based on convolutional kernels and modified U-Net model, Comput. Methods Progr. Biomed. 205 (2021) 106081, https://doi.org/10.1016/j.cmpb.2021.106081.

[28] J.V.B. Soares, J.J.G. Leandro, R.M.C. Junior, H.F. Jelinek, M.J. Cree, Retinal vessel segmentation using the 2D gabor wavelet and supervised classification, IEEE Trans. Med. Imag. 25 (9) (2006) 1214–1222, https://doi.org/10.1109/TMI.2006.879967.

[29] M.F. Aslan, M. Ceylan, A. Durdu, Segmentation of retinal blood vessel using gabor filter and extreme learning machines, 2018 International Conference on Artificial Intelligence and Data Processing (IDAP), IEEE (2018), https://doi.org/10.1109/IDAP.2018.8620890.

[30] H. Boudegga, Y. Elloumi, M. Akil, M. Hedi Bedoui, R. Kachouri, A.B. Abdallah, Fast and efficient retinal blood vessel segmentation method based on deep learning network, Comput. Med. Imag. Graph. 90 (2021) 101902, https://doi.org/10.1016/j.compmedimag.2021.101902.

[31] F. Guo, D. Xiang, Z. Beiji, Z. Chengzhang, S. Wang, Retinal blood vessel segmentation using extreme learning machine, J. Adv. Comput. Intell. Intell. Inf. 21 (7) (2017), https://doi.org/10.20965/jaciii.2017.p1280.

[32] L. Fang, L. Zhang, Y. Yao, Retina blood vessels segmentation based on the combination of the supervised and unsupervised methods, Multidimens. Syst. Signal Process. (32) (2020) 1123–1139, https://doi.org/10.1007/s11045-021-00777-w, 0123456789.

[33] S. Dash, M.R. Senapati, P.K. Sahu, P.S. Chowdary, Illumination normalized based technique for retinal blood vessel segmentation, Int. J. Imag. Syst. Technol. 31 (1) (2021) 351–363, https://doi.org/10.1002/ima.22461.

[34] N. Ibrahim, A. El Farag, R. Kadry, Gaussian blur through parallel computing, Proceedings of the International Conference on Image Processing and Vision Engineering 511 (1) (2021) 978–989, https://doi.org/10.5220/0010513301750179.

[35] K. Geethalakshmi, V.S. Meenakshi, Mathematical morphology and optimum principal curvature based segmentation of blood vessels in human retinal fundus images, Int. J. Innovative Technol. Explor. Eng. 8 (12) (2019) 2278–3075.

[36] J. Dash, N. Bhoi, Retinal blood vessel segmentation using otsu thresholding with principal component analysis, 2018 2nd international conference on inventive systems and control (ICISC), IEEE (2018), https://doi.org/10.1109/ICISC.2018.8398938.

[37] W. Liu, H. Yang, T. Tian, Z. Cao, X. Pan, W. Xu, Y. Jin, F. Gao, Full-resolution network and dual-threshold iteration for retinal vessel and coronary angiograph segmentation, IEEE Journal of Biomedical and Health Informatics 26 (9) (2022) 4623–4634, https://doi.org/10.1109/JBHI.2022.3188710.

[38] G. Feudjio, T.B. Saha, D. Tchiotsop, An accurate unsupervised extraction of retinal vasculature using curvelet transform and classical morphological operators, Comput. Biol. Med. 178 (2024) 108801, https://doi.org/10.1016/j.compbiomed.2024.108801.

[39] A.D. Rahulkar, D.V. Jadhav, R.S. Holqmbe, Fast discrete curvelet transform based anisotropic feature extraction for iris recognition, ICTACT Journal on Image and Video Processing 2 (2010) 69–75, https://doi.org/10.21917/ijivp.2010.0010.

[40] E. Candès, L. Demanet, D. Donoho, L. Ying, Fast discrete curvelet transforms, Multiscale Model. Simul. 5 (3) (2006) 861–899, https://doi.org/10.1137/05064182X.

[41] A. Altan, S. Karasu, Recognition of covid-19 disease from x-ray images by hybrid model consisting of 2D curvelet transform, chaotic salp swarm algorithm and deep learning technique, Chaos, Solit. Fractals 140 (2020) 110071, https://doi.org/10.1016/j.chaos.2020.110071.

[42] A.W. Setiawan, T.R. Mengko, O.S. Santoso, A.B. Suksmono, Color retinal image enhancement using CLAHE, International Conference on ICT for Smart, Society (2013) 1–3, https://doi.org/10.1109/ICTSS.2013.6588092.

[43] M. Tavakoli, P. Kelley, M. Nazar, F. Kalantari, Automated fovea detection based on unsupervised retinal vessel segmentation method, 2017 IEEE Nuclear Science Symposium and Medical Imaging Conference (NSS/MIC) (2017), https://doi.org/10.1109/NSSMIC.2017.8533061.
[44] L. Zhang, M. Fisher, W. Wang, Retinal vessel segmentation using gabor filter and textons, Medical Image Understanding and Analysis (MIUA 2014) (2014) 155–160.
[45] A. Agresti, Categorical Data Analysis, John Wiley & Sons, 2012, p. 792.
[46] A.E. Ilesanmi, T. Ilesanmi, A.G. Gbotoso, A systematic review of retinal fundus image segmentation and classification methods using convolutional neural networks, Healthcare Analytics 100261 (2023), https://doi.org/10.1016/j.health.2023.100261.
[47] P. Grégory, C. Janick, F.S. Ivo, Coupling image restoration and segmentation: a generalized linear model/bregman perspective, International Journal of Computer Vision Aims and scope 104 (2013) 69–93, https://doi.org/10.1007/s11263-013-0615-2.
[48] E.F. Schisterman, D. Faraggi, B. Reiser, J. Hu, Youden index and the optimal threshold for markers with mass at zero, Stat. Med. 27 (2) (2008) 297–315, https://doi.org/10.1002/sim.2993.
[49] Z. Jadoon, S. Ahmad, M.A.K. Jadoon, A. Imtiaz, N. Muhammad, Z. Mahmood, Retinal blood vessels segmentation using isodata and high boost filter, 3rd International Conference on Computing, Mathematics and Engineering Technologies (iCoMET) 29 (2020 Jan) 1–6, https://doi.org/10.1109/iCoMET48670.2020.9074128. IEEE.
[50] B. Khomri, A. Christodoulidis, L. Djerou, M.C. Babahenini, F. Cheriet, Retinal blood vessel segmentation using the elite guided multiobjective artificial bee colony algorithm, IET Image Process. 12 (12) (2018) 2163–2171, https://doi.org/10.1049/iet-ipr.2018.5425.
[51] B.S. Tchinda, D. Tchiotsop, M. Noubom, V. Louis-Dorr, D. Wolf, Retinal blood vessels segmentation using classical edge detection filters and the neural network, Inform. Med. Unlocked 23 (2021) 100521, https://doi.org/10.1016/j.imu.2021.100521.
[52] K. Hu, Z. Zhenzhen, N. Xiaorui, Z. Yuan, C. Chunhong, X. Fen, G. Xieping, Retinal vessel segmentation of color fundus images using multiscale convolutional neural network with an improved cross-entropy loss function, Neurocomputing 309 (2018) 179–191, https://doi.org/10.1016/j.neucom.2018.05.011.
[53] Z. Yan, Y. Xin, C. Kwang-Ting, Joint segment-level and pixel-wise losses for deep learning based retinal vessel segmentation, IEEE (Inst. Electr. Electron. Eng.) Trans. Biomed. Eng. 65 (9) (2018) 1912–1923, https://doi.org/10.1109/TBME.2018.2828137.
[54] J. Zhang, D. Behdad, B. Erik, J.P.W. Pluim, D. Remco, B.M. ter Haar Romeny, Robust retinal vessel segmentation via locally adaptive derivative frames in orientation scores, IEEE Trans. Med. Imag. 35 (12) (2016) 2631–2644, https://doi.org/10.1109/TMI.2016.2587062.
[55] G. Azzopardi, S. Nicola, V. Mario, P. Nicolai, Trainable cosfire filters for vessel delineation with application to retinal images, Med. Image Anal. 19 (1) (2015) 46–57, https://doi.org/10.1016/j.media.2014.08.002.
[56] Y. Kejuan, B. Zou, Z. Chen, Q. Liu, Retinal vessel segmentation using dense u-net with multiscale inputs, J. Med. Imag. 6 (3) (2019), https://doi.org/10.1117/1.JMI.6.3.034004.
[57] Y.Q. Zhao, X.H. Wang, X.F. Wang, F.Y. Shih, Retinal vessels segmentation based on level set and region growing, Pattern Recogn. 47 (7) (2014) 2437–2446, https://doi.org/10.1016/j.patcog.2014.01.006.
[58] M.M. Fraz, B. Abdul, S.A. Barman, Application of morphological bit planes in retinal blood vessel extraction, J. Digit. Imag. 26 (2) (2013) 274–286, https://doi.org/10.1007/s10278-012-9513-3.
[59] D.A. Dharmawan, D. Li, B.P. Ng, S. Rahardja, A new hybrid algorithm for retinal vessels segmentation on fundus images, IEEE Access 7 (2019) 41885–41896, https://doi.org/10.1109/ACCESS.2019.2906344.
[60] M.M. Fraz, P. Remagnino, A. Hoppe, B. Uyyanonvara, A.R. Rudnicka, C.G. Owen, S.A. Barman, An ensemble classification-based approach applied to retinal blood vessel segmentation, IEEE (Inst. Electr. Electron. Eng.) Trans. Biomed. Eng. 59 (9) (2012) 2538–2548, https://doi.org/10.1109/TBME.2012.2205687.
[61] R. Vega, G. Sanchez-Ante, L.E. Falcon-Morales, H. Sossa, E. Guevara, Retinal vessel extraction using lattice neural networks with dendritic processing, Comput. Biol. Med. 58 (2015) 20–30, https://doi.org/10.1016/j.compbiomed.2014.12.016.
[62] S. Aslani, H. Sarnel, A new supervised retinal vessel segmentation method based on robust hybrid features, Biomed. Signal Process Control 30 (2016) 1–12, https://doi.org/10.1016/j.bspc.2016.05.006.
[63] T. Mapayi, S. Viriri, J.R. Tapamo, Adaptive thresholding technique for retinal vessel segmentation based on GLCM-energy information, Comput. Math. Methods Med. 2015 (2015), https://doi.org/10.1155/2015/597475.
[64] F. Farokhain, C. Yang, H. Demirel, S. Wu, I. Beheshti, Automatic parameters selection of Gabor filters with the imperialism competitive algorithm with application to retinal vessel segmentation, Biocybern. Biomed. Eng. 37 (1) (2017) 246–254, https://doi.org/10.1016/j.bbe.2016.12.007.
[65] A.M. Mendonca, A. Campilho, Segmentation of retinal blood vessels by combining the detection of centerlines and morphological reconstruction, IEEE Trans. Med. Imag. 25 (9) (2006) 1200–1213, https://doi.org/10.1109/TMI.2006.879955.
[66] X. You, Q. Peng, Y. Yuan, Y.-M. Cheung, J. Lei, Segmentation of retinal blood vessels using the radial projection and semi-supervised approach, Pattern Recogn. 44 (10–11) (2011) 2314–2324, https://doi.org/10.1016/j.patcog.2011.01.007.
[67] B.S. Lam, Y. Gao, A.W.-C. Liew, General retinal vessel segmentation using regularization-based multiconcavity modeling, IEEE Trans. Med. Imag. 29 (7) (2010) 1369–1381, https://doi.org/10.1109/TMI.2010.2043259.
[68] D. Marín, A. Aquino, M.E. Gegoendez-Arias, J.M. Bravo, A new supervised method for blood vessel segmentation in retinal images by using gray-level and moment invariants-based features, IEEE Trans. Med. Imag. 30 (1) (2011) 146–158, https://doi.org/10.1109/TMI.2010.2064333.
[69] Y. Lin, H. Zhang, G. Hu, Automatic retinal vessel segmentation via deeply supervised and smoothly regularized network, IEEE Access 7 (2018) 57717–57724, https://doi.org/10.1109/ACCESS.2018.2844861.
[70] F. Farokhian, C. Yang, H. Demirel, S. Wu, I. Beheshti, Automatic parameters selection of Gabor filters with the imperialism competitive algorithm with application to retinal vessel segmentation, Biocybern. Biomed. Eng. 37 (1) (2017) 246–254, https://doi.org/10.1016/j.bbe.2016.12.007.
[71] M. Alhussein, K. Aurangzeb, S.I. Haider, An unsupervised retinal vessel segmentation using hessian and intensity based approach, IEEE Access 8 (2020) 165056–165070, https://doi.org/10.1109/ACCESS.2020.3022943.
[72] S. Dash, S. Verma, N.Z. Jhanjhi, M. Masud, M. Baz, Curvelet transform based on edge preserving filter for retinal blood vessel segmentation, Comput. Mater. Continua (CMC) 71 (2) (2022), https://doi.org/10.32604/cmc.2022.020904.
[73] S. Dash, M.R. Senapati, Enhancing detection of retinal blood vessels by combined approach of DWT, Tyler Coye and Gamma correction, Biomed. Signal Process Control 57 (2020) 101740, https://doi.org/10.1016/j.bspc.2019.101740.
[74] T.A. Soomro, A. Ali, N.A. Jandan, A.J. Afifi, M. Irfan, S. Alqhtani, A. Glowacz, A. Alqahtani, R. Tadeusiewicz, E. Kantoch, L. Zheng, Impact of novel image preprocessing techniques on retinal vessel segmentation, Electronics 10 (18) (2021) 2297, https://doi.org/10.3390/electronics10182297.
[75] S. Dash, S. Verma, Bevinakoppa S. Kavita, M. Wozniak, J. Shafi, M.F. Ijaz, Guidance image-based enhanced matched filter with modified thresholding for blood vessel extraction, Symmetry 14 (2) (2022) 194, https://doi.org/10.3390/sym14020194.